Voxelwise and Patientwise Correlation of ^{18}F-FDOPA PET, Relative Cerebral Blood Volume, and Apparent Diffusion Coefficient in Treatment-Naïve Diffuse Gliomas with Different Molecular Subtypes

Hiroyuki Tatekawa[1,2], Akifumi Hagiwara[1,2], Jingwen Yao[1–3], Talia C. Oughourlian[1,2,4], Issei Ueda[2], Hiroyuki Uetani[2], Catalina Raymond[1,2], Albert Lai[5,6], Timothy F. Cloughesy[5,6], Phioanh L. Nghiemphu[5,6], Linda M. Liau[5,7], Whitney B. Pope[2], Noriko Salamon[2], and Benjamin M. Ellingson[1–5]

[1]UCLA Brain Tumor Imaging Laboratory, Center for Computer Vision and Imaging Biomarkers, David Geffen School of Medicine, UCLA, Los Angeles, California; [2]Department of Radiological Science, David Geffen School of Medicine, UCLA, Los Angeles, California; [3]Department of Bioengineering, Henry Samueli School of Engineering, UCLA, Los Angeles, California; [4]Neuroscience Interdepartmental Program, David Geffen School of Medicine, UCLA, Los Angeles, California; [5]UCLA Neuro-Oncology Program, David Geffen School of Medicine, UCLA, Los Angeles, California; [6]Department of Neurology, David Geffen School of Medicine, UCLA, Los Angeles, California; and [7]Department of Neurosurgery, David Geffen School of Medicine, UCLA, Los Angeles, California

Our purpose was to identify correlations between ^{18}F-fluorodihydroxyphenylalanine (^{18}F-FDOPA) uptake and physiologic MRI, including relative cerebral blood volume (rCBV) and apparent diffusion coefficient (ADC), in gliomas with different molecular subtypes and to evaluate their prognostic values. **Methods:** Sixty-eight treatment-naïve glioma patients who underwent ^{18}F-FDOPA PET and physiologic MRI were retrospectively selected (36 with isocitrate dehydrogenase wild-type [IDH$_{wt}$], 16 with mutant 1p/19q noncodeleted [IDH$_{m-noncodel}$], and 16 with mutant codeleted [IDH$_{m-codel}$]). Fluid-attenuated inversion recovery hyperintense areas were segmented and used as regions of interest. For voxelwise and patientwise analyses, Pearson correlation coefficients ($r_{voxelwise}$ and $r_{patientwise}$) between the normalized SUV (nSUV), rCBV, and ADC were evaluated. Cox regression analysis was performed to investigate the associations between overall survival and $r_{voxelwise}$, maximum or median nSUV, median rCBV, or median ADC. **Results:** For IDH$_{wt}$ and IDH$_{m-noncodel}$ gliomas, nSUV demonstrated significant positive correlations with rCBV ($r_{voxelwise}$ = 0.25 and 0.31, respectively; $r_{patientwise}$ = 0.50 and 0.70, respectively) and negative correlations with ADC ($r_{voxelwise}$ = −0.19 and −0.19, respectively; $r_{patientwise}$ = −0.58 and −0.61, respectively) in both voxelwise and patientwise analyses. IDH$_{m-codel}$ gliomas demonstrated a significant positive correlation between nSUV and ADC only in voxelwise analysis ($r_{voxelwise}$ = 0.18). In Cox regression analysis, $r_{voxelwise}$ between nSUV and rCBV (hazard ratio, 28.82) or ADC (hazard ratio, 0.085) had significant associations with overall survival for only IDH$_{wt}$ gliomas. **Conclusion:** IDH$_{m-codel}$ gliomas showed distinctive patterns of correlations between amino acid PET and physiologic MRI. Stronger correlations between nSUV and rCBV or ADC may result in a worse prognosis for IDH$_{wt}$ gliomas.

MRI is the imaging modality of choice for clinical evaluation of gliomas because of its high spatial resolution, its significant contrast in soft tissues, and a lack of ionizing radiation. Various advanced sequences to evaluate physiologic status, such as perfusion imaging, diffusion-weighted imaging (DWI), spectroscopy, and functional MRI, can be readily acquired during clinical examinations. Amino acid PET, such as with ^{18}F-fluorodihydroxyphenylalanine (^{18}F-FDOPA) and ^{18}F-fluorethyltyrosine, is often used in neurooncologic practices to identify metabolically active tumor tissues. These amino acid PET examinations provide information that complements MRI, and the combination of PET and MRI metrics was reported to be useful for clinical management of gliomas (*1,2*). Hybrid examinations of PET and MRI have recently been performed for evaluating gliomas in clinical practice (*3*). Hence, knowledge of their imaging features and association of their findings are instrumental for clinical treatment and prediction of prognosis.

Although some previous studies, such as perfusion imaging or DWI, have correlated amino acid PET and physiologic MRI (*4,5*), most studies demonstrated complementary and partially congruent information in PET and physiologic MRI. These correlation studies often evaluated representative MRI features, including the maximum, mean, median, or minimum values, within a specific tumor region such as the contrast-enhanced or focal hypermetabolic area. However, only a few studies have performed an unbiased evaluation of the voxelwise correlations between amino acid PET and physiologic MRI within a whole tumor. Previous voxelwise analyses have reported a positive correlation between ^{18}F-fluorethyltyrosine uptake and relative cerebral blood volume (rCBV) (*6*) and a negative correlation between ^{18}F-FDOPA uptake and apparent diffusion

coefficient (ADC) in grade III and IV gliomas (7). Hence, amino acid PET and physiologic MRI may depict partially overlapping pathophysiologic features.

In 2016, the World Health Organization (WHO) classification of tumors of the central nervous system was modified to include molecular subtypes, such as isocitrate dehydrogenase (IDH) gene mutation and chromosomal 1p/19q codeletion, for brain tumor classification (8). These molecular subtypes have proven to be essential for determining treatment decisions and prognosis. However, there have been no studies evaluating the correlations of amino acid PET with physiologic MRI in different molecular subtypes or the associations of their correlations with patient prognosis. We hypothesize that these correlations may differ among different tumor subtypes and affect prognosis. The objectives of this study were to reveal the correlations between ^{18}F-FDOPA uptake, rCBV, and ADC in treatment-naïve gliomas with different molecular subtypes, especially IDH mutation and 1p/19q codeletion status, and to evaluate the associations of their correlations and patient prognoses.

MATERIALS AND METHODS

Patient Selection

Sixty-eight treatment-naïve and histologically confirmed glioma patients who underwent ^{18}F-FDOPA PET and MRI between 2007 and 2019 were retrospectively selected. The selected MR images were acquired within 2 mo of the corresponding PET images. The MRI scans consisted of at least pre- and postcontrast T1-weighted images and T2-weighted fluid-attenuated inversion recovery (FLAIR) images. Perfusion imaging for 61 subjects and DWI for 63 subjects were performed. The median date between the PET scan and surgery or biopsy was 16 d (range, 1–505 d). No patients underwent stereotactic biopsy before ^{18}F-FDOPA PET or MRI. Patients were classified by IDH mutational status and 1p/19q codeletion status, which were detected by conventional techniques (9). When available, O^6-methylguanine-DNA methyltransferase (MGMT) promoter methylation status and epidermal growth factor receptor (EGFR) amplification status were obtained as supplemental information. The overall survival (OS) was measured from the time of the PET scans until death or the censored dates (median interval, 721 d), with 18 subjects who were deceased at the time of analysis. The study was approved by the institutional review board, and all subjects signed an informed consent form. Table 1 summarizes the patient demographics and molecular information, and Supplemental Table 1 describes each patient in more detail (supplemental materials are available at http://jnm.snmjournals.org).

Acquisition of MRI

Anatomic MRI consisted of standard T1-weighted pre- and postcontrast images (2-dimensional axial turbo spin-echo images with a slice thickness of 3 mm and no interslice gap, or 3-dimensional inversion-prepared gradient-echo images with an isotropic voxel size of 1–1.5 mm), and T2-weighted FLAIR images at a 3-mm slice thickness with no interslice gap from a 1.5-T or 3-T clinical MRI scanner.

For dynamic susceptibility contrast perfusion MRI, a total dose of 0.1 mmol/kg of gadolinium-DTPA or gadolinium-BTDO3A (Magnevist or Gadavist; Bayer Healthcare Pharmaceuticals) was administered with 0.025 mmol/kg of the preload dosage to mitigate T1-based leakage contamination, and the remaining 0.075 mmol/kg was used for dynamic bolus administration as previously described (10). A 2-min gap was allowed between the preload dose and the start of the baseline dynamic susceptibility contrast-enhanced MRI. The dynamic susceptibility contrast-enhanced MRI was acquired with an echo time/repetition time of 21–23/1,250–1,290 ms, a flip angle of 60°, a 128 × 128 matrix, and a slice thickness of 5 mm, with no interslice gap. The number of baseline acquisitions before contrast agent injection was 10–25, and number of

TABLE 1
Patient Demographics and Molecular Information

Demographic	Data
Total patients	68 (100%)
Female patients	26 (38.2%)
Age ± SD (y)	51.7 ± 14.9
WHO classification grade	
II	29 (42.6%)
III	25 (36.8%)
IV	14 (20.6%)
IDH and 1p/19q status	
IDH$_{wt}$	36 (52.9%)
IDH$_{m-noncodel}$	16 (23.5%)
IDH$_{m-codel}$	16 (23.5%)
MGMT-promoter methylation status	
Unmethylated	27 (39.7%)
Methylated	27 (39.7%)
Unknown	14 (20.6%)
EGFR amplification status	
Negative	38 (55.9%)
Positive	11 (16.2%)
Unknown	19 (27.9%)
Surgical procedure	
Biopsy	12 (17.6%)
Subtotal resection	44 (64.7%)
Gross total resection	12 (17.6%)

Qualitative data are numbers and percentages; continuous data are mean and SD.

time points was 120. First, dynamic time-series images were motion-corrected using the FSL software (mcflirt; FMRIB [http://www.fmrib.ox.ac.uk/fsl/]). Second, rCBV maps were calculated using a bidirectional contrast agent leakage-correction algorithm, to model the contrast flux into and out of the vasculature. Finally, a normalized rCBV map was computed by dividing the rCBV map by the median rCBV of regions of interest (ROIs) placed on the contralateral normal-appearing white matter.

Before injection of the contrast agent, DWI was performed using a single-shot echo-planar imaging sequence in the axial plane for 9 patients, with a repetition time/echo time of 3,000–10,400/77–93 ms, a 128 × 128 matrix, and a slice thickness of 3 mm with no interslice gap. ADC maps were calculated from the acquired DWI with b = 1,000 s/mm^2 and b = 0 s/mm^2 images and expressed in units of 10^{-6} mm^2/s. Diffusion tensor imaging data were collected for 54 patients for whom conventional DWI was not obtained. Mean diffusivity maps were used as estimates of ADCs after motion correction using the FSL software (dtifit). The parameters of the diffusion tensor imaging consisted of 12–64 equidistant diffusion-sensitizing directions with b = 1,000 s/mm^2, along with a single b = 0 s/mm^2 image with a repetition time/echo time of 4,500–11,500/79–93 ms, a 128 × 128 matrix, and a slice thickness of 2 mm with no interslice gap.

Acquisition of ^{18}F-FDOPA PET

^{18}F-FDOPA PET images were acquired using a high-resolution full-ring PET scanner (ECAT-HR; Siemens), after the subjects fasted for more than 4 h. Following previously established procedures, ^{18}F-FDOPA was synthesized and injected intravenously (11). CT images

were acquired before the PET images for attenuation correction. Three-dimensional ^{18}F-FDOPA emission data were acquired for a total of 30 min, and the data were integrated between 10 and 30 min after injection to obtain 20-min static ^{18}F-FDOPA images after reconstruction. PET images were reconstructed using an ordered-subsets expectation maximization iterative reconstruction algorithm consisting of 6 iterations with 8 subsets (*12*). Finally, a gaussian filter with a full width at a half maximum of 4 mm was applied. The resulting voxel size was $1.34 \times 1.34 \times 3$ mm for the ^{18}F-FDOPA PET images. SUV maps for ^{18}F-FDOPA were based on the radioactivity divided by the decay-corrected injected dose per body mass (*13*). The resulting SUV images were then normalized (nSUV) to the median value of the striatum as previously described (*14*).

Postprocessing and ROI Analysis

All MRI and PET images were registered to the postcontrast T1-weighted images for each patient using a 6°-of-freedom rigid transformation and a mutual-information cost function using the FSL software (flirt). To register the ADC maps, we rigidly aligned b = 0 s/mm^2 images acquired during the DWI or diffusion tensor imaging sequence to the postcontrast T1-weighted images and applied the transform matrices to the ADC maps. When needed, manual alignment was performed with FreeSurfer software (tkregister2; Massachusetts General Hospital [https://surfer.nmr.mgh.harvard.edu]). A single ROI (FLAIR$_{ROI}$) was segmented on the basis of the hyperintense regions on the T2-weighted FLAIR images by a board-certified neuroradiologist (13 y of clinical experience) with Analysis of Functional NeuroImages software (National Institute of Mental Health Scientific and Statistical Computing Core [https://afni.nimh.nih.gov]) using a semiautomatic procedure as previously described (*15*).

Statistical Analyses

The maximum nSUV, median nSUV, median rCBV, and median ADC within FLAIR$_{ROI}$ were assessed between the different molecular subtypes by 1-way ANOVA and Student t testing or by Kruskal–Wallis and Mann–Whitney U tests.

For voxelwise analysis, nSUV, rCBV, and ADC within FLAIR$_{ROI}$ were compared using Pearson correlation coefficients ($r_{voxelwise}$) for each patient. The correlation coefficients were evaluated for each molecular subtype to determine whether the 95% CI of mean values included zero. These correlation coefficients were also compared for the different molecular subtypes using ANOVA and Student t testing. To account for interindividual variation, a linear mixed-effects model (fixed slope and random intercept) was also used, given by the following equation:

$$rCBV_{im} \ (\text{or } ADC_{im}) \ = \ \beta_0 + \beta_1 nSUV_{im} + b_{0m} + \varepsilon_{im},$$

Eq. 1

where $rCBV_{im}$ (or ADC_{im}) and $nSUV_{im}$ represent rCBV (or ADC) and ^{18}F-FDOPA measurements, respectively, of voxel i in patient m. β denotes the fixed effects, b_{0m} is the random effect for patient m (i.e., patient- or acquisition-specific), and ε_{im} is the observation error (*6*). Additionally, the areas under the receiver-operating-characteristic curves, along with sensitivity and specificity, were analyzed to evaluate the discriminatory ability of $r_{voxelwise}$ between different molecular subtypes.

For the patientwise analysis, Pearson correlation coefficients ($r_{patientwise}$) between median nSUV, median rCBV, and median ADC were calculated. The Fisher r-to-z transformation was used to compare the strength of $r_{patientwise}$ between the different molecular subtypes.

Cox multivariate regression analyses controlling for age were performed to investigate the association of OS with maximum nSUV, median nSUV, median rCBV, and median ADC, as well as for $r_{voxelwise}$ between nSUV, rCBV, and ADC. Kaplan–Meier curves and log-rank tests were used to differentiate short- and long-term survival for gliomas stratified by the median $r_{voxelwise}$.
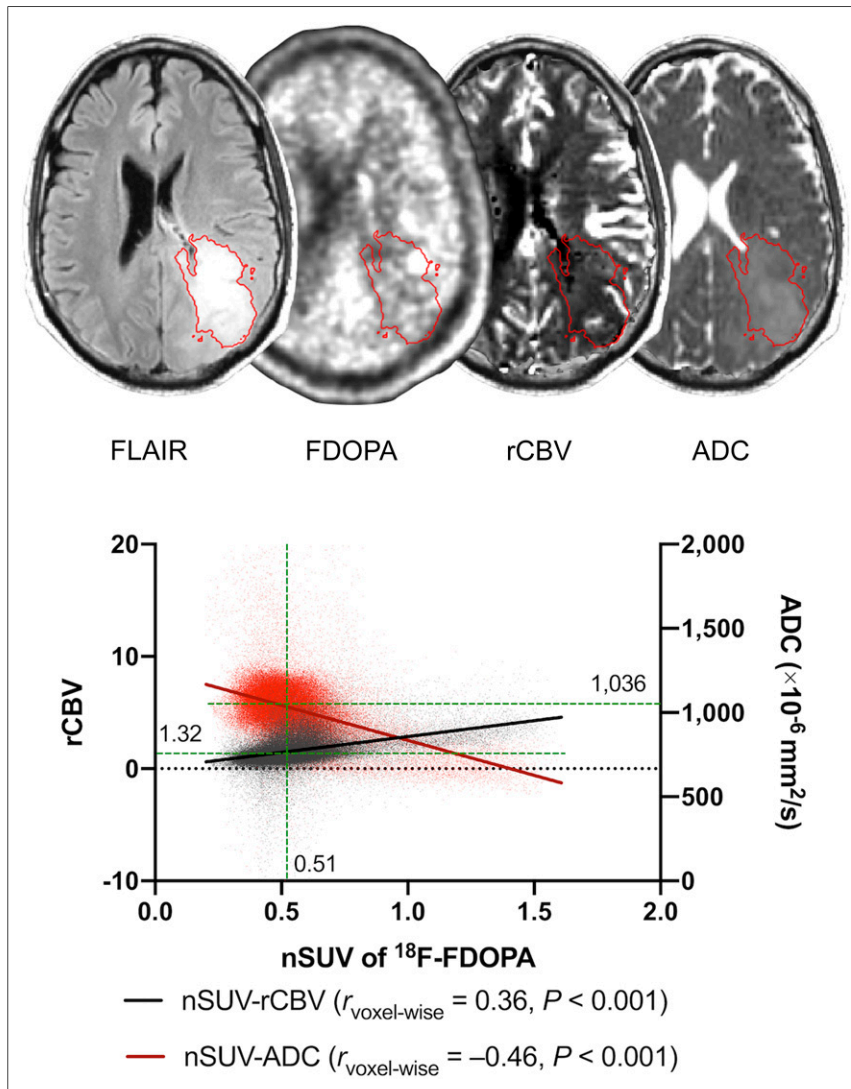

FIGURE 1. Example of postprocessing and segmentation in 36-y-old man with treatment-naïve WHO grade IV, IDH$_{wt}$, MGMT-unmethylated, and EGFR-amplified glioblastoma. ROIs of FLAIR hyperintense region are overlaid on ^{18}F-FDOPA, rCBV, and ADC maps. A scatterplot extracted from ROI is shown with $r_{voxelwise}$ between nSUV and rCBV or ADC. Median nSUV, rCBV, and ADC (green lines) are also shown.

TABLE 2
^{18}F-FDOPA PET and Physiologic MRI Data in IDH$_{wt}$, IDH$_{m-noncodel}$, and IDH$_{m-codel}$ Gliomas

| | Tumor type | | | P | | | |
Parameter	IDH$_{wt}$	IDH$_{m-noncodel}$	IDH$_{m-codel}$	ANOVA	IDH$_{wt}$ vs. IDH$_{m-noncodel}$	IDH$_{wt}$ vs. IDH$_{m-codel}$	IDH$_{m-noncodel}$ vs. IDH$_{m-codel}$
Maximum nSUV	1.64 ± 0.75	1.15 ± 0.30	1.56 ± 0.92	0.024*†	0.007*‡	0.46‡	0.07‡
Median nSUV	0.78 ± 0.27	0.65 ± 0.15	0.83 ± 0.19	0.012*	0.08	0.48	0.004*
Median rCBV	1.70 ± 0.76	1.15 ± 0.37	1.42 ± 0.29	0.014*	0.009*	0.2	0.43
Median ADC ($\times 10^{-6}$ mm^2/s)	1015 ± 152	1241 ± 193	1169 ± 110	<0.001*	<0.001*	0.001*	0.22

*Statistically significant.
†Kruskal–Wallis test.
‡Mann–Whitney U test.
Data are mean ± SD.

Statistical analysis was performed using MATLAB (version R2019b; MathWorks) and GraphPad Prism (version 8.3; GraphPad Software). Statistical significance was defined at a P value of less than 0.05, and no correction for multiple comparisons was performed.

RESULTS

The current study included 68 treatment-naïve glioma patients (26 women) with a mean age of 51.7 y at the time of the PET examination. According to the 2007/2016 WHO criteria, 14 gliomas were grade IV, 25 were grade III, and 29 were grade II; 36 gliomas were IDH wild-type (IDH$_{wt}$), 16 were IDH mutant 1p/19q noncodeleted (IDH$_{m-noncodel}$), and 16 were IDH mutant 1p/19q codeleted (IDH$_{m-codel}$); 27 gliomas were MGMT-unmethylated, 27 were MGMT-methylated, and the remaining 14 did not have the MGMT status available; 38 gliomas were EGFR amplification–negative, 11 were EGFR amplification–positive, and the remaining 19 did not have the EGFR status available.

Figure 1 illustrates an example of a segmented FLAIR$_{ROI}$ and a voxelwise analysis between nSUV and rCBV or ADC in a 36-y-old man. This patient had a WHO grade IV, IDH$_{wt}$, MGMT-unmethylated, and EGFR amplification–positive glioblastoma and showed a positive voxelwise correlation between nSUV and rCBV and a negative voxelwise correlation between nSUV and ADC. The median nSUV, rCBV, and ADC within the FLAIR$_{ROI}$ were also calculated for the patientwise analyses.

Table 2 shows the extracted values of the ^{18}F-FDOPA and physiologic MRI. The maximum nSUV was significantly higher in the IDH$_{wt}$ gliomas than in the IDH$_{m-noncodel}$ gliomas (P = 0.007), whereas the median nSUV was significantly higher in the IDH$_{m-codel}$ gliomas than in the IDH$_{m-noncodel}$ gliomas (P = 0.004). The median rCBV was significantly higher in the IDH$_{wt}$ gliomas than in the IDH$_{m-noncodel}$ gliomas (P = 0.009), whereas the median ADC was significantly lower in the IDH$_{wt}$ gliomas than in either the IDH$_{m-noncodel}$ (P < 0.001) or the IDH$_{m-codel}$ gliomas (P = 0.001).

The IDH$_{wt}$ and IDH$_{m-noncodel}$ gliomas demonstrated significant positive correlations between nSUV and rCBV (Figs. 2 and 3; IDH$_{wt}$, $r_{voxelwise}$ = 0.25, CI = [0.17, 0.32], and $r_{patientwise}$ = 0.50, CI = [0.19, 0.73]; IDH$_{m-noncodel}$, $r_{voxelwise}$ = 0.31, CI = [0.23, 0.39], and $r_{patientwise}$ = 0.70, CI = [0.33, 0.89]) in both voxelwise and patientwise analyses. They also exhibited significant negative correlations between nSUV and ADC (IDH$_{wt}$, $r_{voxelwise}$ = −0.19, CI = [−0.28,

−0.10], and $r_{patientwise}$ = −0.58, CI = [−0.77, −0.30]; IDH$_{m-noncodel}$, $r_{voxelwise}$ = −0.19, CI = [−0.31, −0.06], and $r_{patientwise}$ = −0.61, CI = [−0.85, −0.15]). The IDH$_{m-codel}$ gliomas demonstrated a significant positive correlation between nSUV and ADC in the voxelwise analysis. Other voxelwise and patientwise correlations between nSUV and rCBV or ADC did not show statistical significance (between nSUV and rCBV, $r_{voxelwise}$ = 0.07, CI = [−0.03, 0.16], and $r_{patientwise}$ = 0.18, CI = [−0.41, 0.66]; between nSUV and ADC, $r_{voxelwise}$ = 0.18, CI = [0.04, 0.31], and $r_{patientwise}$ = 0.17, CI = [−0.38, 0.64]). When $r_{voxelwise}$ was compared among different molecular subtypes, the $r_{voxelwise}$ between nSUV and rCBV was significantly lower (P = 0.008 and < 0.001) and the $r_{voxelwise}$ between nSUV and ADC was significantly higher in IDH$_{m-codel}$ than in IDH$_{wt}$ and IDH$_{m-noncodel}$ gliomas (P < 0.001 for both). When the strengths of $r_{patientwise}$ were compared among the different molecular subtypes, there were no significant differences between median nSUV and rCBV (P > 0.09 for all). The patientwise correlation between median nSUV and ADC was significantly weaker in IDH$_{m-codel}$ than in IDH$_{wt}$ (P = 0.016) or IDH$_{m-noncodel}$ (P = 0.032). Because grade IV gliomas
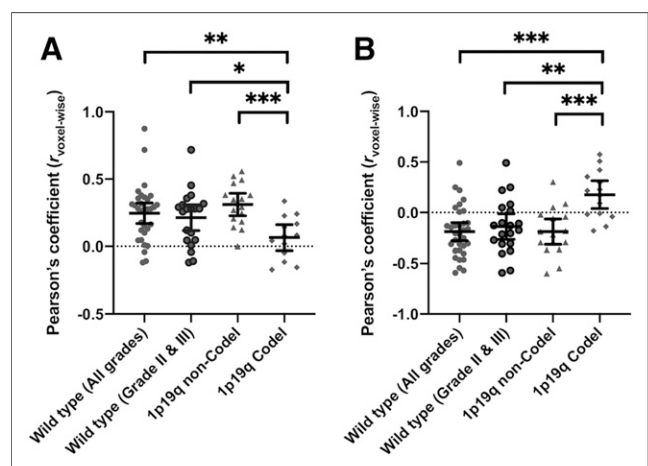

FIGURE 2. $r_{voxelwise}$ between nSUV and rCBV (A) and between ^{18}F-FDOPA uptake and ADC (B). All comparisons with ANOVA have P values of less than 0.002. Bars denote mean value and 95% CI. *Mean P < 0.05. **Mean P < 0.01. ***Mean P < 0.001.
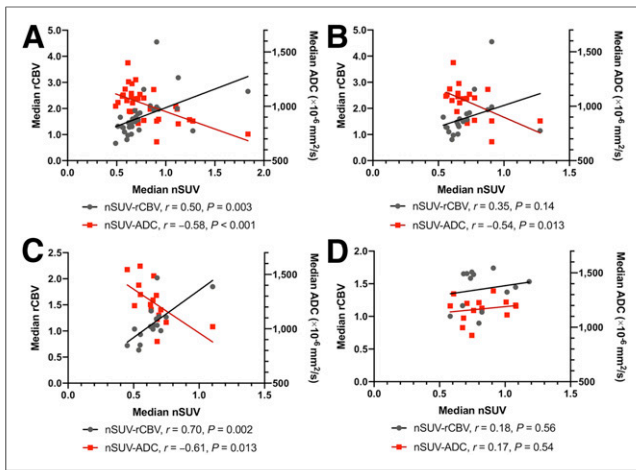
FIGURE 3. $r_{patientwise}$ between median nSUV and rCBV or ADC in IDH$_{wt}$ (all grades) (A), IDH$_{wt}$ (grades II and III) (B), IDH$_{m-noncodel}$ (C), and IDH$_{m-codel}$ (D). There are no significant differences in strength of correlation coefficients for median nSUV and rCBV among different molecular subtypes. Correlation coefficient of median nSUV and ADC is significantly weaker in IDH$_{m-codel}$ than in IDH$_{wt}$ (all grades, $P = 0.016$; grades II and III, $P = 0.042$) or IDH$_{m-noncodel}$ ($P = 0.032$).

were included in only the IDH$_{wt}$ group, voxelwise and patientwise analyses were performed on only lower-grade IDH$_{wt}$ gliomas (grades II and III; $n = 22$). The cohort with lower-grade IDH$_{wt}$ exhibited voxelwise trends similar to those of the cohort that included all IDH$_{wt}$ grades. However, no significant patientwise correlation between nSUV and rCBV was observed (IDH$_{wt}$ with lower grade, between nSUV and rCBV, $r_{voxelwise} = 0.22$, CI = [0.12, 0.31], and $r_{patientwise} = 0.35$, CI = [−0.11, 0.68]; between nSUV and ADC, $r_{voxelwise} = −0.14$, CI = [−0.27, −0.01], and $r_{patientwise} = −0.54$, CI = [−0.80, −0.13]). The voxelwise and patientwise analyses between rCBV and ADC are described in Supplemental Figure 1.

In a linear mixed-effects model (Supplemental Table 2), the mean slope (β_1) for the prediction of rCBV by nSUV (fixed effect) was 1.24, 2.52, and 0.76 in IDH$_{wt}$, IDH$_{m-noncodel}$, and IDH$_{m-codel}$, respectively. The mean slope (β_1) for the prediction of ADC by nSUV was −157, −649, and 187 in IDH$_{wt}$, IDH$_{m-noncodel}$, and IDH$_{m-codel}$, respectively. All slopes (β_1) of the mixed-effects model were consistent with the voxelwise and patientwise analyses.

The receiver-operating-characteristic analysis differentiated IDH$_{m-codel}$ from IDH$_{wt}$ and IDH$_{m-noncodel}$ gliomas, with area under the curve, sensitivity, and specificity of 0.80, 63%, and 92%, respectively, for $r_{voxelwise}$ between nSUV and rCBV; 0.86, 76%, and 86%, respectively, for $r_{voxelwise}$ between nSUV and ADC; and 0.68, 69%, and 73%, respectively, for $r_{voxelwise}$ between rCBV and ADC (Fig. 4). The differentiation between IDH$_{wt}$ and IDH$_{m}$ gliomas is shown in Supplemental Figure 2.

Because no patients in the IDH$_{m-noncodel}$ group and only 1 patient in the IDH$_{m-codel}$ group had died, only the IDH$_{wt}$ gliomas ($n = 36$) were included in the Cox regression analysis and log-rank test. The Cox multivariate analysis controlling for age (Table 3) demonstrated significant associations in hazard with the $r_{voxelwise}$ between nSUV and rCBV (hazard ratio, 28.82; $P = 0.017$) and between nSUV and ADC (hazard ratio, 0.085; $P = 0.038$). The significant associations did not change when controlling for age and surgical procedure (resection or biopsy). The Kaplan–Meier curves and log-rank tests showed a significant difference in OS ($P = 0.049$) when IDH$_{wt}$ gliomas were stratified by the median

value of $r_{voxelwise}$ between nSUV and ADC, with a lower $r_{voxelwise}$ associated with worse survival (Supplemental Fig. 3).

The voxelwise and patientwise analyses between different MGMT methylation statuses or between different EGFR amplification statuses are summarized in Supplemental Figures 4 and 5 and Supplemental Tables 3 and 4.

DISCUSSION

In this study, voxelwise and patientwise correlations between ^{18}F-FDOPA uptake, rCBV, and ADC were evaluated among different molecular subtypes. For IDH$_{wt}$ and IDH$_{m-noncodel}$ gliomas, nSUV and rCBV had significant positive correlations, whereas nSUV and ADC had significant negative correlations. In contrast, IDH$_{m-codel}$ gliomas demonstrated a significant positive correlation between nSUV and ADC in the voxelwise analysis, which was an inverse relationship identified in IDH$_{wt}$ or IDH$_{m-noncodel}$ gliomas. No other correlations in IDH$_{m-codel}$ gliomas showed a statistical significance. $r_{voxelwise}$ could discriminate IDH$_{m-codel}$ from IDH$_{m-noncodel}$ gliomas with high accuracy (area under the curve, 0.88 for $r_{voxelwise}$ between nSUV and ADC). The Cox regression analysis revealed that the $r_{voxelwise}$ between nSUV and rCBV or ADC had a significant association with OS for IDH$_{wt}$ gliomas.

The results suggest that the physiologic features of IDH$_{m-codel}$ gliomas may differ from those of IDH$_{wt}$ or IDH$_{m-noncodel}$ gliomas. In the 2016 WHO classification of tumors of the central nervous system, oligodendrogliomas are defined by the presence of both IDH mutation and 1p/19q codeletion (8). IDH$_{m-codel}$ oligodendrogliomas showed higher amino acid tracer uptake, higher rCBV, and lower ADC than IDH$_{m-noncodel}$ diffuse astrocytomas (16). These physiologic imaging features are compatible with our
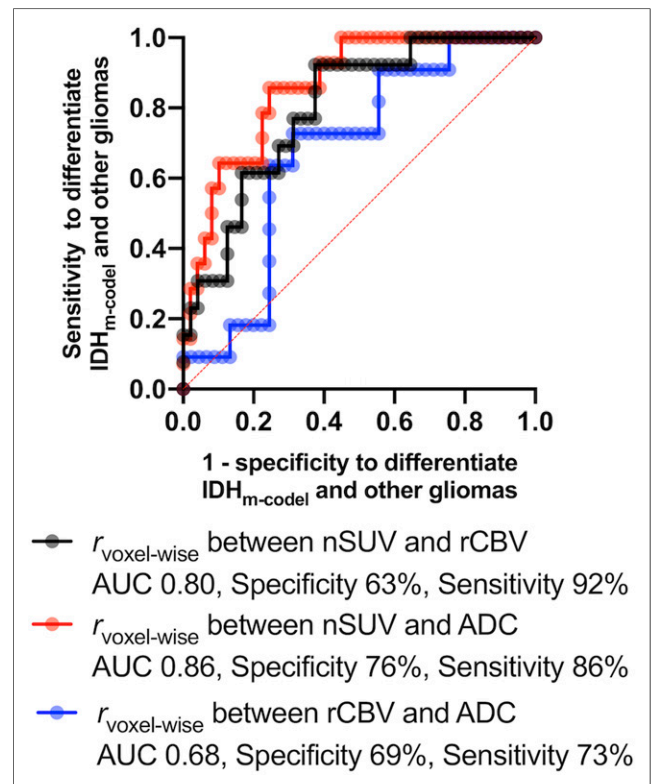

FIGURE 4. Receiver-operating-characteristic curve to differentiate IDH$_{m-codel}$ from IDH$_{wt}$ and IDH$_{m-noncodel}$ gliomas. AUC = area under curve.

TABLE 3
Cox Multivariate Regression Controlling for Age in IDH_{wt}

Parameter	Hazard ratio	95% CI	P
Maximum nSUV	1.341	0.737–2.443	0.33
Median nSUV	0.83	0.109–6.342	0.86
Median rCBV	1.184	0.666–2.104	0.56
Median ADC ($\times 10^{-6}$ mm²/s)	0.998	0.995–1.002	0.33
$r_{voxelwise}$ between nSUV and rCBV	28.82	1.828–454.4	0.017*
$r_{voxelwise}$ between nSUV and ADC	0.085	0.008–0.874	0.038*
$r_{voxelwise}$ between rCBV and ADC	0.099	0.005–1.970	0.13

*Statistically significant.

results, although some results were not statistically significant. The uptake of amino acid tracers in oligodendrogliomas is known to reflect transportation mediated by amino acid carriers over the endothelial cell membrane and to correlate with the microvessel and cell density of the tumor (17). The presence of a branching network of delicate capillaries (chicken-wire pattern) or the frequent cortical involvement of oligodendrogliomas relative to astrocytomas may cause a relatively higher rCBV (18–20). Oligodendrogliomas are often highly cellular in the central regions, with closely packed, relatively small cells (18), which may result in relatively lower ADCs. These pathologic features and anatomic localization may reflect the physiologic imaging features of oligodendrogliomas.

However, in less cellular areas at the periphery of oligodendrogliomas, diffuse infiltrative growth can be pathologically easily identified, often with prominent secondary structure formation, including clustering of tumor cells around the perikarya of preexisting neurons under the pial surface, and surrounding cortical small vessels (18). A previous voxelwise histogram analysis also reported higher vascular heterogeneity in oligodendrogliomas than in astrocytomas (16). Such intratumoral, diverse, and heterogeneous pathologic features of oligodendrogliomas may have resulted in an inverse correlation to other gliomas or no correlations between ^{18}F-FDOPA uptake and rCBV or ADC.

In the current study, the $r_{voxelwise}$ between nSUV and rCBV or ADC had a significant association with OS in IDH_{wt} gliomas. Gross tumor heterogeneity shown by histogram and texture analyses of PET has been suggested to be associated with survival in patients with gliomas (21,22). However, the results of these studies were incongruent in terms of gross tumor heterogeneity, and it was difficult to understand the microstructural underpinnings: higher contrast and busyness, indicating higher heterogeneity, were associated with worse survival; however, higher kurtosis and coarseness, indicating less heterogeneity, were also associated with worse survival. In contrast, to the best of our knowledge, our study is the first to show the contribution of voxel-level heterogeneity to survival. Cell proliferation, development, and maintenance with an adequate blood supply by angiogenesis are essential for tumor growth and invasion (17,23,24). Previous imaging pathologic correlation studies have shown that rCBV was associated with tumor cell density (23), tumor proliferation (25), and vascularization (26). Regions with a low ADC were also reported to reflect a high mitotic index and tumor cell density (7). In these areas, hypermetabolism indicated by amino acid PET might reflect an accelerated and efficient tumor growth cycle. In contrast, gliomas with

coexisting normal cells of the central nervous system cells, a large extracellular space, or abundant macromolecules such as proteoglycans and adhesion protein may reflect heterogeneous pathologic features (5,27). Gliomas with such heterogeneous features may be associated with weak correlations between physiologic MRI/PET, less efficient growth, and better prognosis.

The current study had some limitations and future directions. First, not all MRI scans were acquired using the same parameters and scanners. Further, differences in patient age and sex may also have affected the ^{18}F-FDOPA uptake (28); however, our approach is supported by the results of the mixed-effects model, which accounts for interindividual variation and demonstrates consistent results with the voxelwise and patientwise correlation analyses. Second, because associations of the imaging correlations and pathologic features were not confirmed, a stereotactic image–histology comparison may be required in a future study. Third, only FLAIR hyperintense ROIs were used for the voxelwise and patientwise analyses; the ROIs of contrast enhancement were not used because only one third of the patients (70% of them were IDH_{wt}) showed contrast enhancement. Furthermore, only the IDH_{wt} group was included in the Cox regression analysis. A study with a larger population including all subtypes or those other than IDH_{wt} may reveal new biomarkers of gliomas. Fourth, although Karnofsky performance status is an important factor in evaluating survival, this status was not available for all subjects and thus was not analyzed in this study. Finally, the existence of necrosis, hemorrhage, and calcification was not considered in this study. If necrosis exists in a tumor, both ^{18}F-FDOPA uptake and rCBV are expected to decrease and ADC is expected to increase. Hence, necrosis may enhance the strength of correlation coefficients between ^{18}F-FDOPA and rCBV or ADC by increasing the range of these metrics. However, hemorrhage may change ADCs over time because of the change in ratio of oxyhemoglobin, deoxyhemoglobin, and hemosiderin. Furthermore, hemosiderin deposition and dense calcification lead to very low ADCs. Although no data were excluded from this study, elimination of outliers in ADCs may increase the prediction performance.

CONCLUSION

In the voxelwise and patientwise analyses, IDH_{wt} and $IDH_{m-noncodel}$ gliomas showed significant positive correlations between ^{18}F-FDOPA uptake and rCBV and significant negative correlations between ^{18}F-FDOPA uptake and ADC. In contrast, $IDH_{m-codel}$

gliomas had either an inverse correlation to other glioma subtypes or no significant correlations between ^{18}F-FDOPA uptake and rCBV or ADC, possibly reflecting the unique pathologic features of heterogeneous or diverse oligodendroglial components. A strong correlation between ^{18}F-FDOPA uptake and rCBV or ADC in IDH$_{wt}$ may contribute to the acceleration of efficient and aggressive tumor growth, resulting in worse prognosis.

DISCLOSURE

KEY POINTS

QUESTION: Is there a correlation between ^{18}F-FDOPA PET and physiologic MRI in different molecular subtypes?

PERTINENT FINDINGS: Specific correlations patterns exist between ^{18}F-FDOPA PET and physiologic MRI in different molecular subtypes.

IMPLICATIONS FOR PATIENT CARE: Correlations between ^{18}F-FDOPA PET and physiologic MRI may predict prognosis.

REFERENCES

1. Galldiks N, Lohmann P, Cicone F, Langen KJ. FET and FDOPA PET imaging in glioma. In: Pope W, ed. *Glioma Imaging*. Springer; 2019:211–222.
2. Verburg N, Koopman T, Yaqub MM, et al. Improved detection of diffuse glioma infiltration with imaging combinations: a diagnostic accuracy study. *Neuro Oncol.* 2020;22:412–422.
3. Deuschl C, Kirchner J, Poeppel TD, et al. ^{11}C-MET PET/MRI for detection of recurrent glioma. *Eur J Nucl Med Mol Imaging.* 2018;45:593–601.
4. Rossi Espagnet MC, Romano A, Mancuso V, et al. Multiparametric evaluation of low grade gliomas at follow-up: comparison between diffusion and perfusion MR with ^{18}F-FDOPA PET. *Br J Radiol.* 2016;89:20160476.
5. Rahm V, Boxheimer L, Bruehlmeier M, et al. Focal changes in diffusivity on apparent diffusion coefficient MR imaging and amino acid uptake on PET do not colocalize in nonenhancing low-grade gliomas. *J Nucl Med.* 2014;55:546–550.
6. Göttler J, Lukas M, Kluge A, et al. Intra-lesional spatial correlation of static and dynamic FET-PET parameters with MRI-based cerebral blood volume in patients with untreated glioma. *Eur J Nucl Med Mol Imaging.* 2017;44:392–397.
7. Karavaeva E, Harris RJ, Leu K, et al. Relationship between [^{18}F]FDOPA PET uptake, apparent diffusion coefficient (ADC), and proliferation rate in recurrent malignant gliomas. *Mol Imaging Biol.* 2015;17:434–442.
8. Louis DN, Perry A, Reifenberger G, et al. The 2016 World Health Organization classification of tumors of the central nervous system: a summary. *Acta Neuropathol (Berl).* 2016;131:803–820.
9. Oughourlian TC, Yao J, Schlossman J, et al. Rate of change in maximum ^{18}F-FDOPA PET uptake and non-enhancing tumor volume predict malignant transformation and overall survival in low-grade gliomas. *J Neurooncol.* 2020;147:135–145.
10. Leu K, Boxerman JL, Lai A, et al. Bidirectional contrast agent leakage correction of dynamic susceptibility contrast (DSC)-MRI improves cerebral blood volume estimation and survival prediction in recurrent glioblastoma treated with bevacizumab. *J Magn Reson Imaging.* 2016;44:1229–1237.
11. Namavari M, Bishop A, Satyamurthy N, Bida G, Barrio JR. Regioselective radiofluorodestannylation with [^{18}F]F2 and [^{18}F]CH3COOF: a high yield synthesis of 6-[^{18}F]fluoro-L-dopa. *Int J Rad Appl Instrum [A].* 1992;43:989–996.
12. Nuyts J, Michel C, Dupont P. Maximum-likelihood expectation-maximization reconstruction of sinograms with arbitrary noise distribution using NEC-transformations. *IEEE Trans Med Imaging.* 2001;20:365–375.
13. Thie JA. Understanding the standardized uptake value, its methods, and implications for usage. *J Nucl Med.* 2004;45:1431–1434.
14. Chen W, Silverman DH, Delaloye S, et al. ^{18}F-FDOPA PET imaging of brain tumors: comparison study with ^{18}F-FDG PET and evaluation of diagnostic accuracy. *J Nucl Med.* 2006;47:904–911.
15. Ellingson BM, Kim HJ, Woodworth DC, et al. Recurrent glioblastoma treated with bevacizumab: contrast-enhanced T1-weighted subtraction maps improve tumor delineation and aid prediction of survival in a multicenter clinical trial. *Radiology.* 2014;271:200–210.
16. Latysheva A, Emblem KE, Brandal P, et al. Dynamic susceptibility contrast and diffusion MR imaging identify oligodendroglioma as defined by the 2016 WHO classification for brain tumors: histogram analysis approach. *Neuroradiology.* 2019;61:545–555.
17. Roodakker KR, Alhuseinalkhudhur A, Al-Jaff M, et al. Region-by-region analysis of PET, MRI, and histology in en bloc-resected oligodendrogliomas reveals intra-tumoral heterogeneity. *Eur J Nucl Med Mol Imaging.* 2019;46:569–579.
18. Wesseling P, van den Bent M, Perry A. Oligodendroglioma: pathology, molecular mechanisms and markers. *Acta Neuropathol (Berl).* 2015;129:809–827.
19. Leu K, Ott GA, Lai A, et al. Perfusion and diffusion MRI signatures in histologic and genetic subtypes of WHO grade II-III diffuse gliomas. *J Neurooncol.* 2017;134:177–188.
20. Guo H, Kang H, Tong H, et al. Microvascular characteristics of lower-grade diffuse gliomas: investigating vessel size imaging for differentiating grades and subtypes. *Eur Radiol.* 2019;29:1893–1902.
21. Pyka T, Gempt J, Hiob D, et al. Textural analysis of pre-therapeutic [^{18}F]-FET-PET and its correlation with tumor grade and patient survival in high-grade gliomas. *Eur J Nucl Med Mol Imaging.* 2016;43:133–141.
22. Mitamura K, Yamamoto Y, Kudomi N, et al. Intratumoral heterogeneity of ^{18}F-FLT uptake predicts proliferation and survival in patients with newly diagnosed gliomas. *Ann Nucl Med.* 2017;31:46–52.
23. Sadeghi N, D'Haene N, Decaestecker C, et al. Apparent diffusion coefficient and cerebral blood volume in brain gliomas: relation to tumor cell density and tumor microvessel density based on stereotactic biopsies. *AJNR Am J Neuroradiol.* 2008;29:476–482.
24. Fischer I, Gagner JP, Law M, Newcomb EW, Zagzag D. Angiogenesis in gliomas: biology and molecular pathophysiology. *Brain Pathol.* 2005;15:297–310.
25. Price SJ, Green HA, Dean AF, Joseph J, Hutchinson PJ, Gillard JH. Correlation of MR relative cerebral blood volume measurements with cellular density and proliferation in high-grade gliomas: an image-guided biopsy study. *AJNR Am J Neuroradiol.* 2011;32:501–506.
26. Hu LS, Eschbacher JM, Dueck AC, et al. Correlations between perfusion MR imaging cerebral blood volume, microvessel quantification, and clinical outcome using stereotactic analysis in recurrent high-grade glioma. *AJNR Am J Neuroradiol.* 2012;33:69–76.
27. Sadeghi N, Camby I, Goldman S, et al. Effect of hydrophilic components of the extracellular matrix on quantifiable diffusion-weighted imaging of human gliomas: preliminary results of correlating apparent diffusion coefficient values and hyaluronan expression level. *AJR.* 2003;181:235–241.
28. Cicone F, Carideo L, Minniti G, Scopinaro F. The mean striatal ^{18}F-DOPA uptake is not a reliable cut-off threshold for biological tumour volume definition of glioma. *Eur J Nucl Med Mol Imaging.* 2019;46:1051–1053.